ACS APPLIED MATERIALS & INTERFACES

Research Article

www.acsami.org

Fabrication of a Ag/Bi_3TaO_7 Plasmonic Photocatalyst with Enhanced Photocatalytic Activity for Degradation of Tetracycline

Bifu Luo, Dongbo Xu, Di Li, Guoling Wu, Miaomiao Wu, Weidong Shi,* and Min Chen*

School of Chemistry and Chemical Engineering, Jiangsu University, Zhenjiang 212013, P. R. China

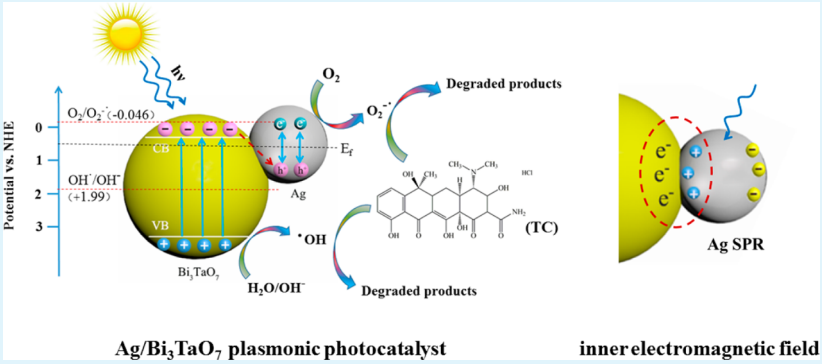

ABSTRACT: A novel Ag/Bi_3TaO_7 plasmonic photocatalyst has been prepared by a simple photoreduction process. The as-prepared Ag/Bi_3TaO_7 photocatalyst exhibited an enhanced photocatalytic activity for the degradation of tetracycline (TC) compared to that of a bare Bi_3TaO_7 catalyst. The 1 wt % Ag-loaded Bi_3TaO_7 sample showed the highest photocatalytic efficiency for TC degradation (85.42%) compared with those of the other samples. The enhanced photocatalytic activity could be ascribed to the synergistic effect of the surface plasmon resonance caused by Ag nanoparticles. Electrochemical impedance spectroscopy demonstrated that the incorporation of silver nanoparticles onto the Bi_3TaO_7 surface promoted the separation of photogenerated carriers. In addition, an electron spin resonance (ESR) and trapping experiment revealed that the photoinduced active species hydroxyl radical and superoxide radical were the main active species in the photocatalytic process of TC degradation. The photocatalytic reaction mechanism was discussed by active species trapping and ESR analysis.

KEYWORDS: *Ag, bismuth tantalate, nanocomposite, SPR, photocatalysis, tetracycline*

1. INTRODUCTION

The widespread use and abuse of antibiotics have aroused particular concern because of their excessive application to human beings, agriculture, and planting.[1,2] As one of the most important antibiotics, tetracycline (TC) is extensively used in human medicine, farming, and aquaculture. Unfortunately, the elimination of TC cannot be completed in the natural environment or biological sewage treatment works.[3,4] Accordingly, an effective technology for attempting to remove TC has become a priority. In recent years, photocatalysis technology has proven to be a good strategy for removing residual pharmaceuticals in waters, which resulted in the formation of superoxide ($^{\bullet}O_2^-$) and hydroxyl ($^{\bullet}OH$) radicals for the decomposition of organic pollutants.[5,6] This provides a promising solution for the transformation and degradation of TC by semiconductor materials. Studies of the photocatalytic degradation of TC using TiO_2, ZnO, and $SrTiO_3$ photocatalysts have been conducted by several researchers.[7−9] However, their practical application is limited as these catalysts are responsive under UV light, which occupies only 4−5% of solar light. It is essential to explore novel photocatalysts with high degradation efficiencies for TC under visible light irradiation.

With an incommensurately modulated fluorite type structure and a band gap of approximately 2.74−2.95 eV, the Bi_3TaO_7 photocatalyst exhibits excellent photocatalytic activity under visible light irradiation.[10] The defect structure of Bi_3TaO_7 exhibits the distorted octahedral geometry with Ta as the central atom. These tantalate octahedra are connected with corner-sharing chains in Bi_3TaO_7.[11] Surface defects and oxygen vacancies can be formed because of the three-dimensional structure of Bi_3TaO_7.[12,13] On the other hand, the valence band (VB) is mainly contributed by O 2p and Bi 6s, resulting in a narrowing of the band gap. Therefore, it has great potential as an attractive photocatalyst for the removal of organic pollutants from domestic or industrial effluent. Nevertheless, its practical application was restricted to the higher level of recombination of the photogenerated electron−hole pairs. Therefore, it is necessary to make some attempts to improve the photocatalytic performance of the Bi_3TaO_7 photocatalyst.

Noble metals have received much attention because of their excellent conductivity and strong electron trapping ability. Moreover, the nanostructures of the modified noble metal could induce surface plasmon resonance (SPR).[14−16] In

Received: April 23, 2015
Accepted: July 13, 2015
Published: July 13, 2015

DOI: 10.1021/acsami.5b03535
ACS Appl. Mater. Interfaces 2015, 7, 17061−17069

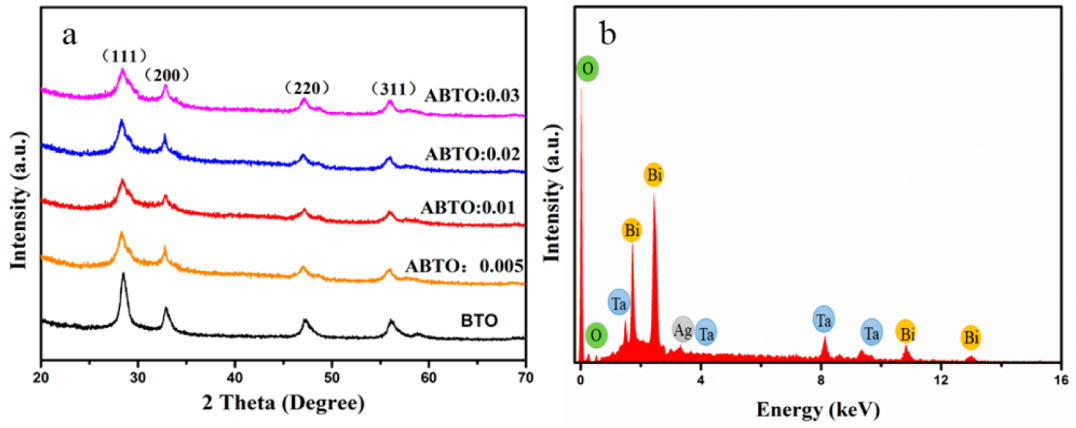

Figure 1. (a) XRD patterns of BTO and ABTO samples. (b) EDX spectra of ABTO:0.01.

comparison with gold or platinum, silver is relatively cheap and exhibits intense local electromagnetic fields caused by SPR, which can accelerate the separation of electrons and holes within a semiconductor. Recently, Ag−TiO_2−graphene ternary nanocomposites were fabricated for photocatalytic hydrogen under visible light.[17] In addition, Ag/AgCl, Ag/Bi_2WO_6, and Ag/TiO_2 composites with enhanced photocatalytic acitivity have been reported.[18−21] Until now, no work was reported for the preparation of the Ag/Bi_3TaO_7 nanocomposite as an efficient visible light-responsive photocatalyst.

Herein, we fabricated a Ag/Bi_3TaO_7 plasmonic photocatalyst to further improve the photocatalytic activity of Bi_3TaO_7. In our work, the Bi_3TaO_7 photocatalyst was prepared via a hydrothermal method, and then Ag was deposited onto Bi_3TaO_7 by a facile photoreduction process with different concentrations of silver nitrate. The photocatalytic properties of Ag/Bi_3TaO_7 photocatalysts were investigated by the degradation of TC under visible light irradiation. Compared to that of pure BTO, Ag/Bi_3TaO_7 nanocomposites revealed excellent TC degradation efficiencies. Among these samples, the ABTO:0.01 sample showed the best photocatalytic activity in the photodegradation of TC. The photocatalytic reaction mechanism was discussed by active species trapping and ESR analysis over the prepared Ag/Bi_3TaO_7 nanocomposite photocatalyst.

2. EXPERIMENTAL SECTION

2.1. Materials. $TaCl_5$ (99.99%) was purchased from Alfa Aesar (Beijing, China), and $AgNO_3$, KOH, $Bi(NO_3)_3{\cdot}5H_2O$, and C_2H_5OH were supplied by Aladdin (Shanghai, China). They are analytically pure and were used without further purification.

2.2. Synthesis of Catalysts. Bi_3TaO_7 was synthesized by following the hydrothermal route. $Bi(NO_3)_3{\cdot}5H_2O$ (5 mmol) and $TaCl_5$ (3 mmol) were dissolved in ethanol (10 mL). The $TaCl_5$ solution was mixed with the $Bi(NO_3)_3$ solution under continuous agitation. A KOH aqueous solution (7 M) was added to the mixture solution and the pH adjusted until the value reached 10.0, and then the mixture was stirred for 30 min to obtain a white slurry. Thereafter, the resultant mixture was sealed in a 50 mL Teflon-lined stainless-steel autoclave with high-temperature resistance and maintained at 220 °C for 24 h. After the system was cooled naturally to room temperature, the yellow precipitate was separated centrifugally and washed three times with distilled water and absolute ethanol. Finally, the obtained product was dried at 60 °C in vacuum for 12 h.

Ag/Bi_3TaO_7 was obtained by a photodeposition method. In a typical synthesis, 0.5 g of Bi_3TaO_7 powder was dispersed in a $AgNO_3$ solution at different concentrations (0.25, 0.5, 1.0, and 1.5 mg/mL). The suspension was stirred for 0.5 h, and then the suspension was illuminated using a 250 W xenon lamp for 60 min. After that, the as-prepared Ag/Bi_3TaO_7 samples were collected by centrifugation and washed with deionized water several times to remove the adsorbed silver ions (Ag^+). Finally, the products were dried in an oven at 60 °C for 12 h. The amounts of Ag were 0, 0.5, 1, 2, and 3% (weight percent). They are denoted BTO, ABTO:0.005, ABTO:0.01, ABTO:0.02, and ABTO:0.03, respectively.

2.3. Characterization. XRD measurements were taken with a Rigaku D/MAX-2500 diffractometer (Cu Kα radiation, λ = 0.1542 nm). The EDX analysis was performed with an F20 S-TWIN electron microscope with an accelerating voltage of 200 kV (SEM, Hitachi). TEM and HRTEM images and SAED were recorded on an F20 S-TWIN electron microscope, operated at 200 kV (Tecnai G2, FEI Co.). Chemical states of the catalyst were examined using XPS spectra (Thermo ESCALAB 250Xi). UV−vis diffused reflectance spectra (DRS) were collected with an UV−vis spectrophotometer (UV2550, Shimadzu). The real content of Ag was detected by atomic absorption spectrophotometry (AAS) (TAS-986). The electron spin resonance (ESR) analysis was conducted with an electron paramagnetic resonance spectrometer (A300-10/12, Bruker). Electrochemical impedance spectra (EIS) was conducted on a CHI 760D workstation.

2.4. Photocatalytic Activity Test. The photocatalytic performance of photocatalysts was evaluated by the degradation of TC under visible light. In each experiment, 50 mg of BTO or ABTO sample was dispersed in an aqueous solution of TC (10 mg/L). Prior to the light irradiation, the suspension was stirred in the dark for 1 h to ensure the adsorption−desorption equilibrium between the photocatalyst and TC. In the process of irradiation, the visible light was generated from a 250 W xenon lamp passed through a UV cutoff filter (λ > 420 nm). During the photocatalytic process, 6 mL of the suspension was withdrawn in a 30 min interval. The concentration of TC in the solution was monitored by UV−vis spectroscopy with absorbance at the characteristic band of 357 nm. The efficiency of degradation was calculated using C/C_0, where C is the concentration of the TC at each irradiated time and C_0 is the initial concentration.

2.5. Kinetic Study of TC Decomposition. To further understand the degradation process, the photocatalytic decomposition kinetics was also investigated. The Langmuir−Hinshelwood (L−H) model can be arranged into the following:[22,23]

$$\ln(C_0/C) \approx k_{app}t$$

where C_0 and C are the adsorption equilibrium and TC concentrations at reaction time t, respectively, and k is the apparent reaction rate constant (inverse minutes).

3. RESULTS AND DISCUSSION

3.1. Crystal Structure and Morphology. The XRD patterns of the as-prepared samples are shown in Figure 1a. All peaks can be indexed to the cubic phase of BTO (JCPDS Card 44-0202) with space group $Fm\bar{3}m$ and the following cell

DOI: 10.1021/acsami.5b03535
ACS Appl. Mater. Interfaces 2015, 7, 17061−17069

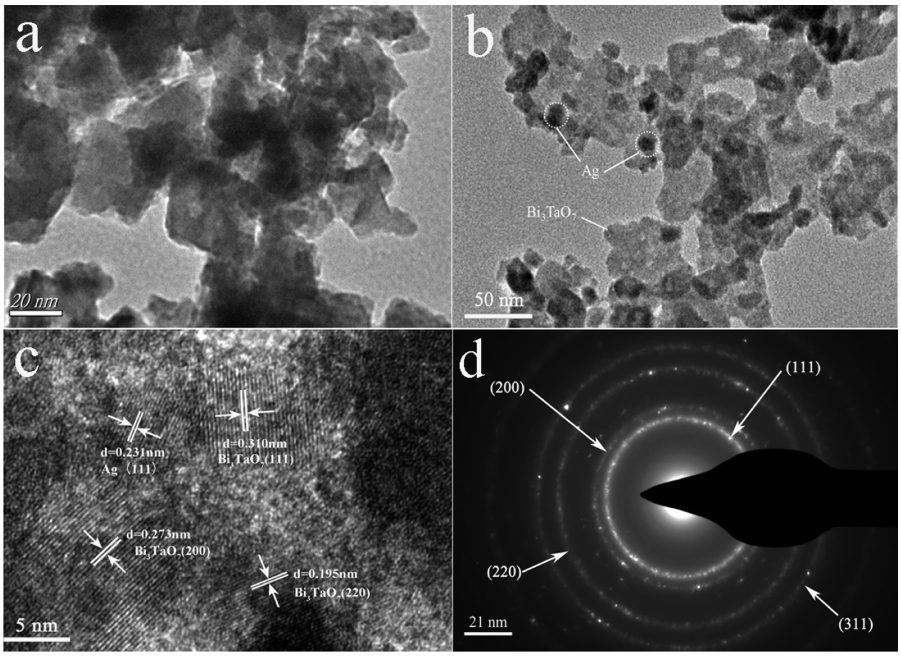

Figure 2. TEM images of (a) BTO and (b) ABTO:0.01. (c) HRTEM image of ABTO:0.01. (d) Selected area electron diffraction (SAED) pattern of BTO.

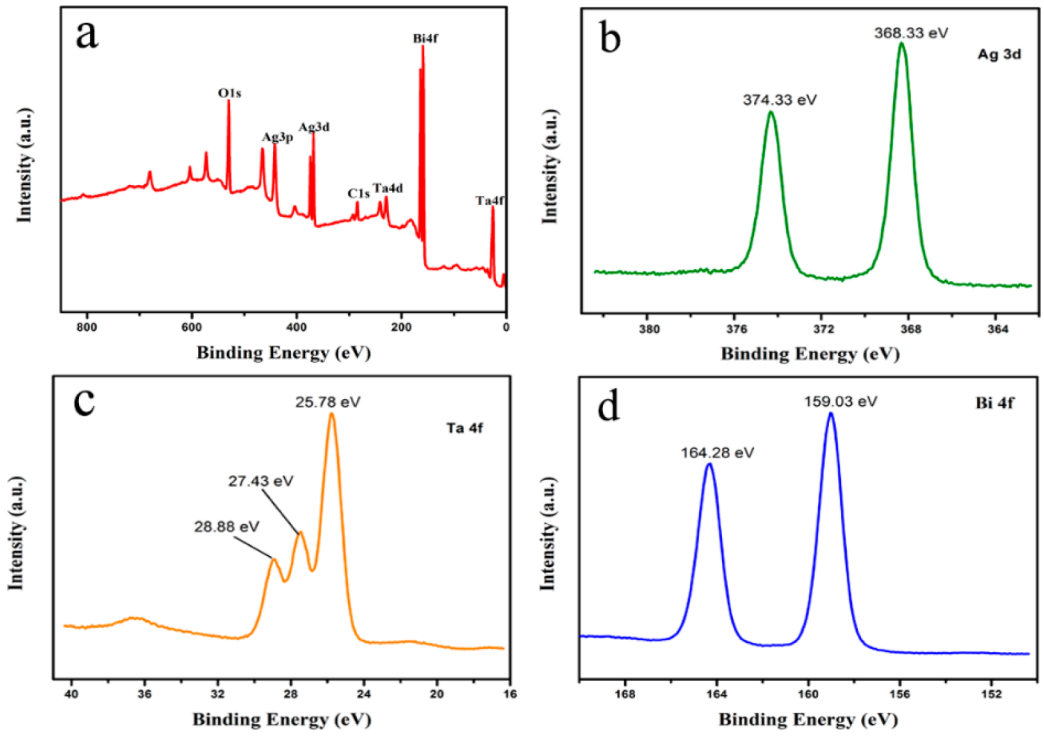

Figure 3. XPS spectra of ABTO:0.01: (a) XPS survey spectrum and XPS spectra of (b) Ag 3d, (c) Ta 4f, and (d) Bi 4f.

parameters: $a = b = c = 5.471$ Å. The XRD patterns of ABTO nanocomposites are similar to those of BTO. No peaks of the Ag phase were identified, probably because the Ag contents are quite low. The signals associated with Bi, Ta, O, and Ag are observed from the EDX image, meaning that Ag nanoparticles are successfully deposited on the surface of BTO (Figure 1b).

TEM and HRTEM images of BTO and ABTO:0.01 are depicted in Figure 2. It is observed that the morphology of BTO is inhomogeneous with edge lengths of 15−40 nm (Figure 2a). In Figure 2b, many smaller Ag nanoparticles are uniformly anchored on the surface of BTO. The size of Ag nanoparticles varied from 10 to 25 nm. In contrast to that of pure BTO, the edge of BTO in ABTO:0.01 seems to stick together, perhaps because of the agglomeration of BTO. It indicates that the presence of Ag has little influence on the structure of BTO. The HRTEM image of the ABTO:0.01 nanocomposite is shown in Figure 2c. There are three interplanar spacings (d = 0.310, 0.273, and 0.195 nm) corresponding to (111), (200), and (220) planes of BTO, respectively. In addition, the lattice fringes of 0.231 nm match

DOI: 10.1021/acsami.5b03535
ACS Appl. Mater. Interfaces 2015, 7, 17061−17069

well to the (111) facet of the Ag nanoparticle. The result further demonstrates the formation of metal Ag. Figure 2d shows the SAED pattern of BTO, the typical partial ring and dot patterns, suggesting that the BTO has a polycrystalline structure. This is consistent with the reports of other groups.[24]

3.2. X-ray Photoelectron Spectra. To verify the surface compositions and oxidation states, further XPS studies were conducted. It is found that the product is mainly composed of Bi, Ta, O, Ag, and C from the entire XPS spectrum (Figure 3a). The binding energy at 284.78 eV is a calibration of C 1s. Two prominent peaks (Figure 3b) at 368.33 and 374.33 eV with a 6 eV spin−orbit splitting value are characteristic of Ag^0 species in the Ag/Bi_3TaO_7 system.[25] The Ta 4f peaks at 28.88 and 27.43 eV (Figure 3c) are ascribed to Ta $4f_{5/2}$, and another peak at 25.78 eV is assigned to Ta $4f_{7/2}$, confirming that Ta exists mainly in the Ta^{5+} form.[26,27] In Figure 3d, the Bi 4f7/2 and Bi 4f5/2 peaks are identified at 159.03 and 164.28 eV, respectively, indicating the presence of Bi with a trivalent oxidation state.[28] The results suggest that there are both Bi_3TaO_7 and Ag species in the composite.

3.3. Real Content of Ag. The actual content of Ag in ABTO samples was detected by atomic absorption spectrometry (AAS). Using a standard curve of Ag^+ in AAS, a silver nitrate solution was prepared with concentrations of 2, 8, 12, 18, and 24 mg/L. Thereafter, 0.2 g ABTO samples were dissolved in 25 mL of aqua regia. Then a 5 mL solution was pipetted into a volumetric flask (50 mL) and diluted with aqua regia to the mark of the volumetric flask. The result is shown in Figure 4. Apparently, the test amounts are smaller than the nominal amounts. One likely reason is that the $AgNO_3$ solution is not completely reduced in the photodeposition process.

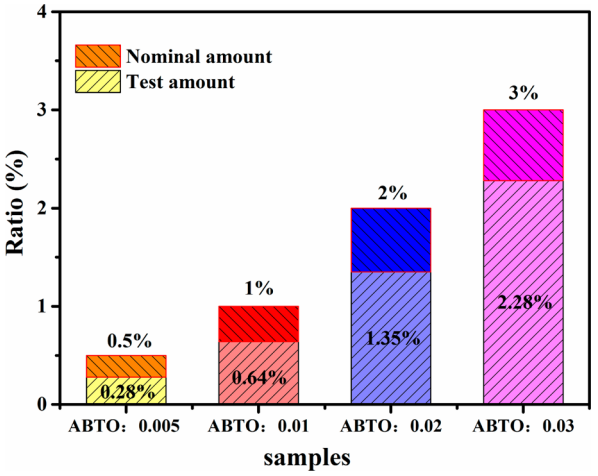

Figure 4. Nominal amounts contrast the test amounts of Ag in ABTO samples.

3.4. UV−Vis Absorption Spectra. The light absorption properties of BTO and ABTO samples are investigated by UV−vis diffuse reflectance spectra. Note that the color of the specimen changed from yellow to brown with the increase in Ag content (Figure 5a). The ABTO nanocomposites show an enhanced photoabsorption property in the visible light region in contrast to bare Bi_3TaO_7, which is attributed to the SPR effect of Ag nanoparticles.[29,30] The band gap energies of Ag/Bi_3TaO_7 with different Ag depositions could be estimated from the Tauc plot. The curve of converted $(\alpha h\nu)^r$ versus $h\nu$ from the UV−vis spectrum, in which α, h, and ν are the absorption coefficient, Planck constant, and light frequency, respectively, and $r = 2$ for a direct band gap material and $r = {}^1/_2$ for an indirect band gap material.[31] It is observed that the energy gap varies from 2.90 to 2.76 eV with the content of Ag increased from 0 to 3% (Figure 5b). The band gap of Bi_3TaO_7 shows a slight change with the Ag loading on the surface of BTO. According to similar studies, this phenomenon might due to the metallic clusters that introduce localized energy levels into the Bi_3TaO_7 band gap.[32,33]

3.5. Photocatalytic Activity for TC Degradation. The photocatalytic activity of the ABTO nanocomposites was evaluated by TC degradation under visible light illumination. The adsorption equilibrium image is shown in Figure 6a. It is noted that TC has reached the adsorption equilibrium within 60 min in the dark. In the absence of the catalysts, the decompposion of TC is negligible. Compared to that of raw BTO, the degradation efficiency exhibits excellent enhancement after the modification of Ag nanoparticles. The Ag proportion plays a significant role in the photocatalytic performance of the ABTO photocatalyst. With the increase in Ag concentration, the photocatalysis capacity increased to a maximal value, after which it decreased upon addition of more Ag nanoparticles. The optimal loading content is determined to be 1%, with the best degradation rate being 85.42% (Figure 6b). This value is ∼1.5-fold higher than that of pristine BTO. However, the excessive Ag nanoparticles may cover up the surface of the samples and suppress the absorption of light, which means a reduction in the number of electrons and holes photogenerated by BTO. Additionally, the formation of excess Ag nanoparticles would occupy a part of the active sites on the surface of BTO and reduce the surface adsorption capability of BTO to the TC molecule, which leads to a decrease in photocatalytic activity.[34,35]

3.6. Kinetic Study. The kinetic behaviors of as-prepared photocatalysts for photodegradation of TC were investigated according to the Langmuir−Hinshelwood model.[36] It is found that the photodegradation process complies with first-order kinetics (Figure 7a). The values of the reaction rate constant (K_{app}) are estimated to be 0.00689, 0.0103, 0.0162, 0.0121, 0.0106, and 0.039 min^{-1}, corresponding to BTO, ABTO:0.005, ABTO:0.01, ABTO:0.02, and ABTO:0.03, respectively. The rate constant of ABTO:0.01 is up to 2.35-fold faster than that of the bare BTO.

3.7. Electrochemical Impedance Spectroscopy. The separation of photogenerated charge carriers can be illustrated by the electrochemical impedance spectra (EIS).[37−39] EIS measurements were performed for bare BTO and the ABTO:0.01 nanocomposite, and the Nyquist plots are shown in Figure 8. The ABTO:0.01 sample exhibits a circular radius smaller than that of pure BTO, which suggests that ABTO:0.01 has a resistance lower than that of pure BTO. The EIS result reveals that the ABTO:0.01 nanocomposite has a preferable efficiency of charge transfer as the modification of Ag nanoparticles.

3.8. Trapping Experiments. To clarify the main active species responsible for TC degradation, free radical trapping experiments were conducted by adding various scavengers to the ABTO:0.01 sample. Herein, 1 mM *p*-benzoquinone (BQ) was utilized for quenching $^{\bullet}O_2^-$, isopropyl (IPA) for $^{\bullet}OH$, and triethanolamine (TEOA) for h^+. The result is shown in Figure 9. The photocatalytic efficiency of TC was affected slightly by the addition of TEOA. However, the photocatalytic activity of ABTO:0.01 is significantly inhibited when BQ or IPA is

DOI: 10.1021/acsami.5b03535
ACS Appl. Mater. Interfaces 2015, 7, 17061−17069

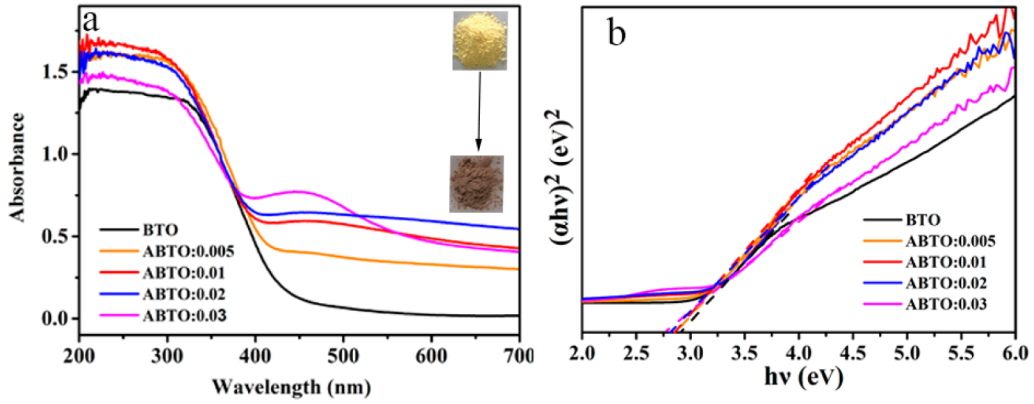

Figure 5. (a) UV−vis diffuse reflectance spectra of different samples. The inset is the color of BTO and ABTO:0.03. (b) Calculated band gap energy by the plot of $(\alpha h\nu)^2$ vs $h\nu$ for different ABTO samples.

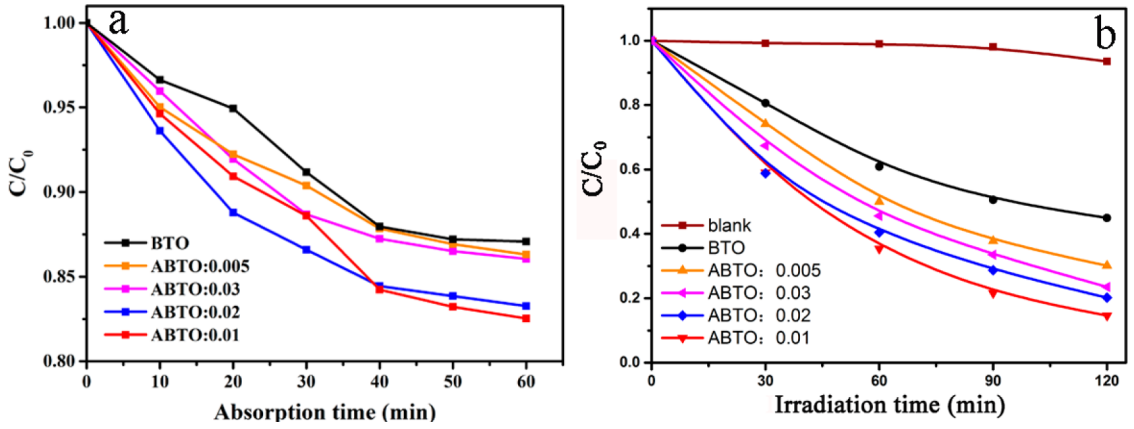

Figure 6. (a) Absorption properties of TC in the dark. (b) Photodecomposition of TC under visible irradiation (λ > 420 nm) over various photocatalysts.

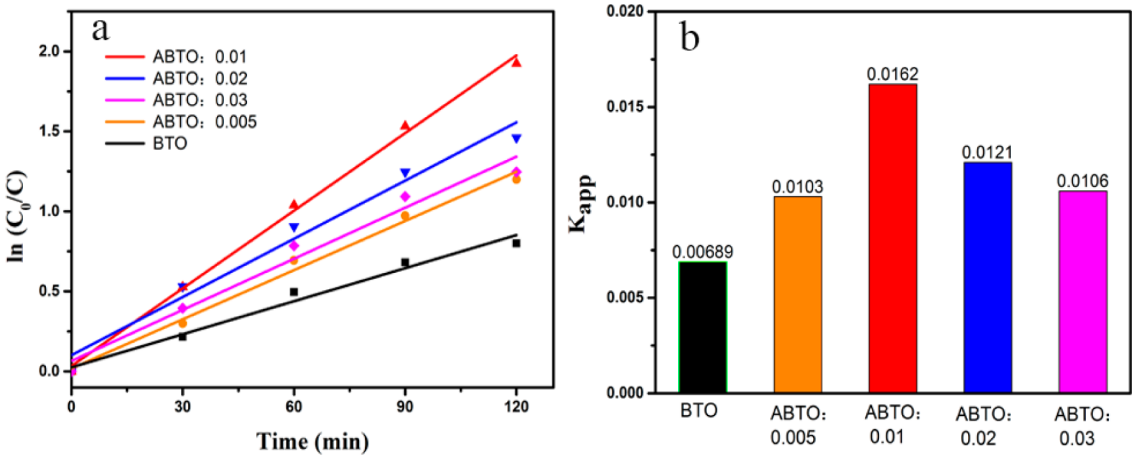

Figure 7. (a) Kinetic curves for the TC photodegradation with pure BTO and ABTO samples. (b) Values of reaction rate constants over BTO and ABTO samples.

introduced into the photocatalytic reaction system. Hence, $^{\bullet}O_2^-$ radicals and $^{\bullet}$OH radicals should be the two main active species during photocatalytic degradation of TC by the ABTO nanocomposites under visible light irradiation.

3.9. Detection of Reactive Oxygen Species by ESR. The ESR technique was further used to detect the presence of $^{\bullet}$OH and $^{\bullet}O_2^-$ radicals in the pure BTO and ABTO:0.01 photocatalytic reaction systems under visible light. From Figure 10a, four characteristic peaks for DMPO−$^{\bullet}$OH adducts were observed (1:2:2:1 quartet pattern) with visible light irradiation (Figure 10a). Furthermore, the $^{\bullet}$OH signal intensities of ABTO:0.01 are obviously stronger than that of pure BTO, suggesting that the amount of $^{\bullet}$OH radicals generated on the ABTO:0.01 surface is larger than that of pure BTO. Similarly, there are four characteristic peaks (Figure 10b) with relative intensities corresponding to the DMPO−$^{\bullet}O_2^-$ adduct, indicating that $^{\bullet}O_2^-$ radicals are also produced during the

DOI: 10.1021/acsami.5b03535
ACS Appl. Mater. Interfaces 2015, 7, 17061−17069

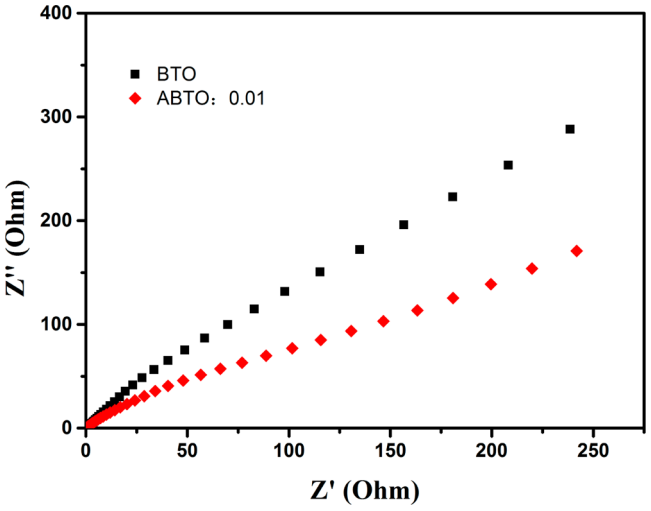

Figure 8. Electrochemical impedance spectra plots of BTO and ABTO:0.01 in a 0.5 M Na_2SO_4 solution (Ag/AgCl electrode).

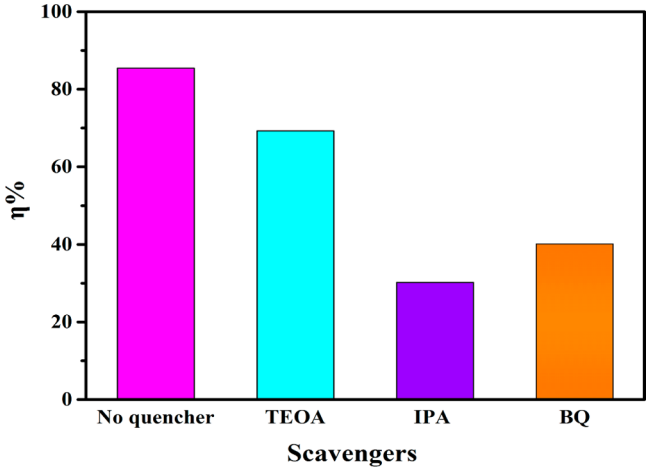

Figure 9. Trapping experiment of the active species for the degradation of TC.

photocatalytic process.[40−42] It is worth mentioning that the characteristic peaks of $^{\bullet}O_2^-$ radicals in BTO are weak, implying that the $^{\bullet}O_2^-$ radicals in BTO can be negligible and more $^{\bullet}O_2^-$ ions are produced after the deposition of Ag. The ESR results confirm that both $^{\bullet}O_2^-$ and $^{\bullet}OH$ are active oxidation species responsible for the photodegradation of TC.

3.10. Evaluation of Stability. The stability and recyclability of the photocatalysts are significant factors in their practical application. As shown in Figure 11a, the recycling experiment for TC decomposition was conducted with an ABTO:0.01 plasmonic photocatalyst. The photocatalyst exhibits a slight loss of activity after five cycles, suggesting that the ABTO:0.01 nanocomposite is a stable photocatalyst for the degradation of TC. The spent catalyst was characterized by XRD (shown in Figure 11b). XRD demonstrates that the catalyst exhibits no obvious change compared with the catalyst before the photocatalytic reaction. As a result, the ABTO nanocomposites are stable and can be easily recycled for their practical application.

3.11. Mechanism of Enhanced Photoactivity. To elucidate the charge separation process of the ABTO nanocomposite, the band positions of Bi_3TaO_7 could be calculated using following equations:[43]

$$E_{CB} = \chi - E^e - 0.5E_g$$

$$E_{VB} = E_g + E_{CB}$$

where E_{VB} and E_{CB} are the valence and conduction band edge potentials, respectively, χ is the absolute electronegativity of the semiconductor, and E^e is defined as the energy of free electrons on the hydrogen scale (~4.5 V vs NHE). Thus, the bottom of CB and the top of VB potentials were calculated to be +0.32 and +3.22 V, respectively. Obviously, the VB potential of the BTO is more positive than the redox potential of OH-/$^{\bullet}OH$ (1.99 V vs NHE) and $H_2O/^{\bullet}OH$ (2.7 V vs NHE). In this case, a large amount of $^{\bullet}OH$ radicals can be formed by the h^+ oxidation of H_2O and OH^-. These as-produced $^{\bullet}OH$ radicals cause oxidation in the process of TC degradation.

Combined with the discussion presented above and the experimental results, a possible mechanism for the degradation of TC with the Ag/Bi_3TaO_7 plasmonic photocatalyst was proposed and is shown in Scheme 1. When the Ag/Bi_3TaO_7 plasmonic photocatalysts are irradiated by the visible light, the electrons in the VB of Bi_3TaO_7 can be excited to the CB, leaving holes in the VB of Bi_3TaO_7. The photoexcited holes stay in the valence band of Bi_3TaO_7 to directly oxidize OH^- or

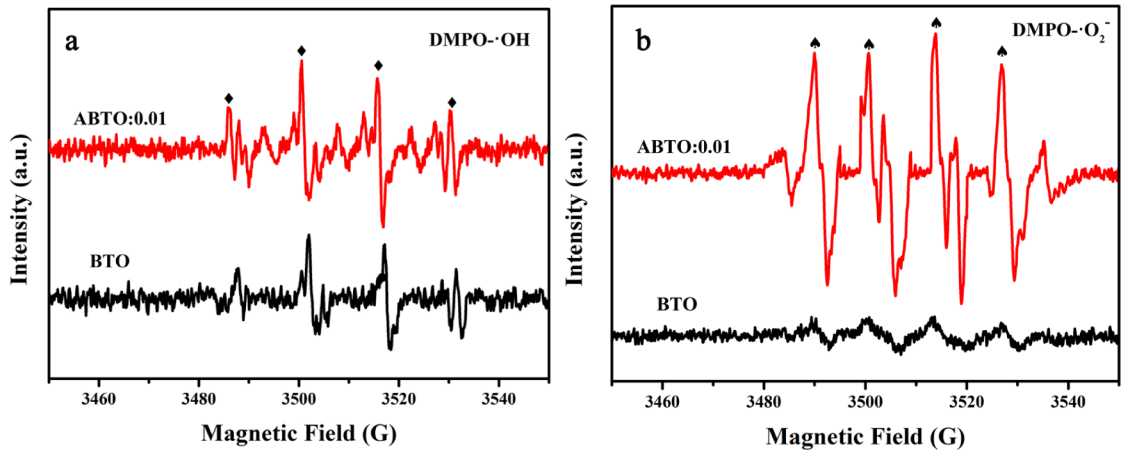

Figure 10. ESR spectra of ABTO:0.01 and BTO with visible light irradiation. (a) DMPO−$^{\bullet}OH$ in aqueous dispersions. (b) DMPO−$^{\bullet}O_2^-$ in methanol dispersions.

DOI: 10.1021/acsami.5b03535
ACS Appl. Mater. Interfaces 2015, 7, 17061−17069

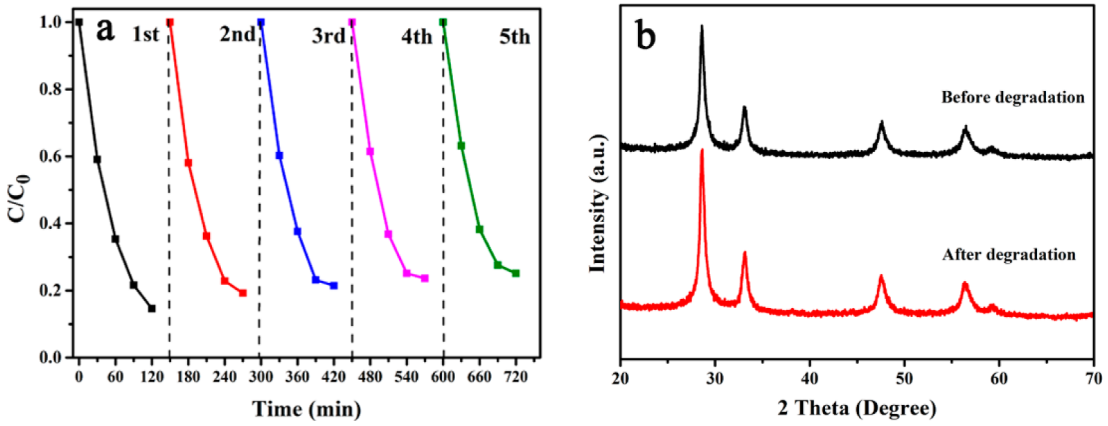

Figure 11. (a) Cycling degradation efficiency of the TC solution in the presence of an ABTO:0.01 sample under visible light irradiation. (b) XRD patterns of ABTO:0.01 before degradation and after degradation for the five cycles.

Scheme 1. Possible Photocatalytic Mechanism for the Degradation of TC on a Ag/Bi_3TaO_7 Plasmonic Photocatalyst

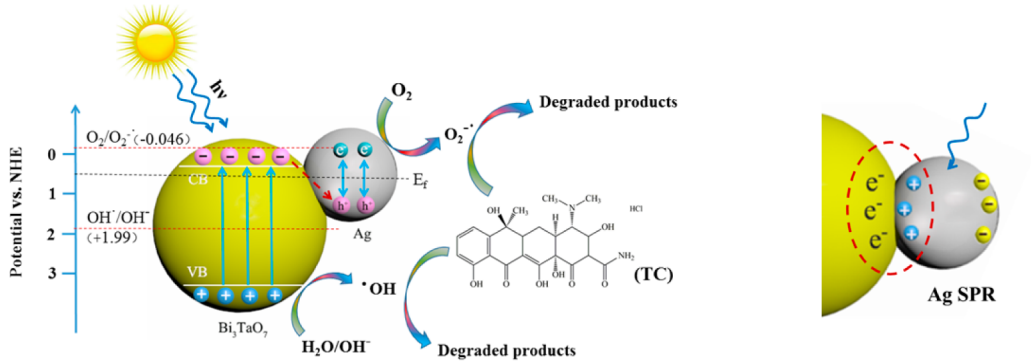

a water molecule to form $^{\bullet}OH$ active species, but the superoxygen radical ($^{\bullet}O_2^-$) cannot be formed because the VB of Bi_3TaO_7 is more positive than that of the $O_2/^{\bullet}O_2^-$ potential (−0.046 V vs NHE). This is confirmed by the ESR result. Simultaneously, the plasmonic absorbance of metallic Ag nanoparticles results in the generation of a large amount of electron−hole (e^-−h^+) pairs,[44,45] as shown in Scheme 1. The photogenerated electrons of Bi_3TaO_7 transfer to the Ag nanoparticles and recombine with the plasmon-induced holes of metallic Ag species for the CB edge potential of Bi_3TaO_7 (0.32 V vs NHE) is more negative than the Fermi level of Ag (0.4 V vs NHE).[46−48] Subsequently, electrons on the Ag nanoparticle can be trapped by adsorbed O_2 in water to produce $^{\bullet}O_2^-$ radical. These radicals are strong oxidants that can oxidize TC to degraded products. As a result, the photocatalytic activity of the Ag/Bi_3TaO_7 nanocomposite can be improved because of the higher separation efficiency of photogenerated carriers.

On the basis of the related literature work and the experimental results described above,[49−51] the process for the enhancement of the photocatalytic activity of Ag/Bi_3TaO_7 nanocomposites can be described as follows:

$$Bi_3TaO_7 + h\nu \rightarrow Bi_3TaO_7(h^+) + Bi_3TaO_7(e^-) \quad (1)$$

$$H_2O \rightarrow H^+ + OH^- \quad (2)$$

$$h^+ + OH^- \rightarrow {}^{\bullet}OH \quad (3)$$

$$e^- + Ag \rightarrow Ag(e^-) \quad (4)$$

$$O_2 + Ag(e^-) \rightarrow {}^{\bullet}O_2^- \quad (5)$$

$$^{\bullet}OH \text{ (or } ^{\bullet}O_2^-) + TC \rightarrow \text{degraded products} \quad (6)$$

4. CONCLUSION

In summary, a novel Ag/Bi_3TaO_7 plasmonic photocatalyst has been successfully fabricated through a simple photoreduction process. The as-prepared Ag/Bi_3TaO_7 nanocomposite photocatalysts exhibit significantly highly visible light photocatalytic activity toward tetracycline degradation. Among these specimens, the ABTO:0.01 sample shows the optimal photocatalytic efficiency. The enhanced photocatalytic activity for the Ag/Bi_3TaO_7 nanocomposite could be ascribed to the SPR absorbance of metallic Ag nanoparticles. The work provides some insight into the design of plasmonic photocatalysts for enhancing visible light-driven photocatalytic activity.

AUTHOR INFORMATION

Corresponding Authors

*E-mail: swd1978@mail.ujs.edu.cn.
*E-mail: chenmin3226@ujs.edu.cn.

Notes

The authors declare no competing financial interest.

DOI: 10.1021/acsami.5b03535
ACS Appl. Mater. Interfaces 2015, 7, 17061−17069

■ ACKNOWLEDGMENTS

This work was supported financially by the National Natural Science Foundation of China (21276116, 21477050, 21301076, 21303074, and 21201085), the Excellent Youth Foundation of Jiangsu Scientific Committee (BK20140011), the Open Project of State Key Laboratory of Rare Earth Resource Utilizations (RERU2014010), the Program for New Century Excellent Talents in University (NCET-13-0835), the Henry Fok Education Foundation (141068), Six Talents Peak Project in Jiangsu Province (XCL-025), and the Chinese-German Cooperation Research Project (GZ1091).

■ REFERENCES

(1) Luo, Y.; Mao, D.; Rysz, M.; Zhou, Q.; Zhang, H.; Xu, L.; J. J. Alvarez, P. Trends in antibiotic Resistance Genes Occurrence in the Haihe River, China. *Environ. Sci. Technol.* **2010**, *44*, 7220−7225.

(2) Yuan, F.; Hu, C.; Hu, X.; Wei, D.; Chen, Y.; Qu, J. Photodegradation and toxicity Changes of Antibiotics in UV and UV/H_2O_2 Process. *J. Hazard. Mater.* **2011**, *185*, 1256−1263.

(3) Önal, A. Overview on Liquid Chromatographic Analysis of Tetracycline Residues in Food Matrices. *Food Chem.* **2011**, *127*, 197−203.

(4) Jing, T.; Wang, Y.; Dai, Q.; Xia, H.; Niu, J.; Hao, Q.; Mei, S.; Zhou, Y. Preparation of Mixed-Templates Molecularly Imprinted Polymers and Investigation of the Recognition Ability for Tetracycline Antibiotics. *Biosens. Bioelectron.* **2010**, *25*, 2218−2224.

(5) Andersen, J. M. Solar and Visible Light-Activated Titania for Removal of Aesticides and Emerging Contaminants: Synergies, Intermediates, and Reusability. Ph.D. Thesis, University of Cincinnati, Cincinnati, OH, 2013.

(6) Han, C.; Pelaez, M.; Likodimos, V.; Kontos, A. G.; Falaras, P.; O'Shea, K.; Dionysiou, D. D. Innovative Visible Light-Activated Sulfur Doped TiO_2 Films for Water Treatment. *Appl. Catal., B* **2011**, *107*, 77−87.

(7) Liu, M.; Qiu, X.; Miyauchi, M.; Hashimoto, K. Energy-Level Matching of Fe(III) Ions Grafted at Surface and Doped in Bulk for Efficient Visible-Light Photocatalysts. *J. Am. Chem. Soc.* **2013**, *135*, 10064−10072.

(8) Li, J.; Lv, S.; Liu, Y.; Bai, J.; Zhou, B.; Hu, X. Photoeletrocatalytic Activity of an n-ZnO/p-Cu_2O/n-TNA Ternary Heterojunction Electrode for Tetracycline Degradation. *J. Hazard. Mater.* **2013**, *262*, 482−488.

(9) Li, P.; Liu, C.; Wu, G.; Heng, Y.; Lin, S.; Ren, A.; Lv, K.; Xiao, L.; Shi, W. Solvothermal Synthesis and Visible Light-Driven Photocatalytic Degradation for Tetracycline of Fe-Doped $SrTiO_3$. *RSC Adv.* **2014**, *4*, 47615−47624.

(10) Zhou, F.; Zhu, Y. Significant Photocatalytic Enhancement in Methylene Blue Degradation of Bi_2WO_6 Photocatalysts Via Graphene Hybridization. *J. Adv. Ceram.* **2012**, *1*, 72−78.

(11) Abrahams, I.; Krok, F.; Struzik, M.; Dygas, J. R. Defect Structure and Electrical Conductivity in Bi_3TaO_7. *Solid State Ionics* **2008**, *179*, 1013−1017.

(12) Subramanian, V.; Wolf, E. E.; Kamat, P. V. Catalysis with TiO_2/Gold Nanocomposites. Effect of Metal Particle Size on the Fermi Level Equilibration. *J. Am. Chem. Soc.* **2004**, *126*, 4943−4950.

(13) Castro, A.; Aguado, E.; Rojo, J.; Herrero, P.; Enjalbert, R.; Galy, J. The New Oxygen-Deficient Fluorite Bi_3NbO_7: Synthesis, Electrical Behavior and Structural Approach. *Mater. Res. Bull.* **1998**, *33*, 31−41.

(14) Pirnat, U.; Valant, M.; Radmilovic, V. Formation Kinetics of a $Bi_3Nb_{1-x}Ta_xO_7$ Fluorite-Type Solid Solution and Thermodynamic Stability of the Bi_3TaO_7 End Member. *J. Am. Ceram. Soc.* **2010**, *93*, 2909−2914.

(15) Testino, A.; Bellobono, I. R.; Buscaglia, V.; Canevali, C.; D'Arienzo, M.; Polizzi, S.; Scotti, R.; Morazzoni, F. Optimizing the Photocatalytic Properties of Hydrothermal TiO_2 by the Control of Phase Composition and Particle Morphology. A Systematic Approach. *J. Am. Chem. Soc.* **2007**, *129*, 3564−3575.

(16) Kuang, D.; Xu, A.; Fang, Y.; Liu, H.; Frommen, C.; Fenske, D. Surfactant-Assisted Growth of Novel PbS Dendritic Nanostructures via Facile Hydrothermal Process. *Adv. Mater.* **2003**, *15*, 1747−1750.

(17) Yang, Y.; Liu, E.; Dai, H.; Kang, L.; Wu, H.; Fan, J.; Hu, X.; Liu, H. Photocatalytic Activity of Ag-TiO_2-Graphene Ternary Nanocomposites and Application in Hydrogen Evolution by Water Splitting. *Int. J. Hydrogen Energy* **2014**, *39*, 7664−7671.

(18) Wang, P.; Huang, B.; Qin, X.; Zhang, X.; Dai, Y.; Wei, J.; Whangbo, M. H. Ag@AgCl: A Highly Efficient and Stable Photocatalyst Active under Visible Light. *Angew. Chem., Int. Ed.* **2008**, *47*, 7931−7933.

(19) Zhang, Z.; Wang, W.; Gao, E.; Sun, S.; Zhang, L. Photocatalysis Coupled with Thermal Effect Induced by SPR on Ag-loaded Bi_2WO_6 with Enhanced Photocatalytic Activity. *J. Phys. Chem. C* **2012**, *116*, 25898−25903.

(20) Awazu, K.; Fujimaki, M.; Rockstuhl, C.; Tominaga, J.; Murakami, H.; Ohki, Y.; Yoshida, N.; Watanabe, T. A Plasmonic Photocatalyst Consisting of Silver Nanoparticles Embedded in Titanium Dioxide. *J. Am. Chem. Soc.* **2008**, *130*, 1676−1680.

(21) Wu, F.; Hu, X.; Fan, J.; Liu, E.; Sun, T.; Kang, L.; Hou, W.; Zhu, C.; Liu, H. Photocatalytic Activity of Ag/TiO_2 Nanotube Arrays Enhanced by Surface Plasmon Resonance and Application in Hydrogen Evolution by Water Splitting. *Plasmonics* **2013**, *8*, 501−508.

(22) Lu, Z.; Luo, Y.; He, M.; Huo, P.; Chen, T.; Shi, W.; Yan, Y.; Pan, J.; Ma, Z.; Yang, S. Preparation and Performance of A Novel Magnetic Conductive Imprinted Photocatalyst for Selective Photodegradation of Antibiotic Solution. *RSC Adv.* **2013**, *3*, 18373−18382.

(23) Zhao, C.; Pelaez, M.; Duan, X.; Deng, H.; O'Shea, K.; Fatta-Kassinos, D.; Dionysiou, D. D. Role of pH on Photolytic and Photocatalytic Degradation of Antibiotic Oxytetracycline in Aqueous Solution under Visible/Solar Light: Kinetics and Mechanism Studies. *Appl. Catal., B* **2013**, *134*−*135*, 83−92.

(24) Zhang, G.; Li, M.; Yu, S.; Zhang, S.; Huang, B.; Yu, J. Synthesis of Nanometer-Size Bi_3TaO_7 and Its Visible-Light Photocatalytic Activity for the Degradation of a 4BS Dye. *J. Colloid Interface Sci.* **2010**, *345*, 467−473.

(25) Stathatos, E.; Lianos, P.; Falaras, P.; Siokou, A. Photocatalytically Deposited Silver Nanoparticles on Mesoporous TiO_2 Films. *Langmuir* **2000**, *16*, 2398−2400.

(26) Xu, D.; Chen, M.; Song, S.; Jiang, D.; Fan, W.; Shi, W. The Synthesis of A Novel Ag-$NaTaO_3$ Hybrid with Plasmonic Photocatalytic Activity under Visible-Light. *CrystEngComm* **2014**, *16*, 1384−1388.

(27) Yan, T.; Zheng, F.; Yu, Y.; Qin, S.; Liu, H.; Wang, J.; Yu, D. Formation Mechanism of Black $LiTaO_3$ Single Crystals through Chemical Reduction. *J. Appl. Crystallogr.* **2011**, *44*, 158−162.

(28) Wang, C.; Zhang, H.; Li, F.; Zhu, L. Degradation and Mineralization of Bisphenol A by Mesoporous Bi_2WO_6 under Simulated Solar Light Irradiation. *Environ. Sci. Technol.* **2010**, *44*, 6843−6848.

(29) Liu, Y.; Fang, L.; Lu, H.; Liu, L.; Wang, H.; Hu, C. Highly Efficient and Stable Ag/Ag_3PO_4 Plasmonic Photocatalyst in Visible Light. *Catal. Commun.* **2012**, *17*, 200−204.

(30) Tang, Y.; Wee, P.; Lai, Y.; Wang, X.; Gong, D.; Kanhere, P. D.; Lim, T.-T.; Dong, Z.; Chen, Z. Hierarchical TiO_2 Nanoflakes and Nanoparticles Hybrid Structure for Improved Photocatalytic Activity. *J. Phys. Chem. C* **2012**, *116*, 2772−2780.

(31) Murphy, A. Band-gap determination from Diffuse Reflectance Measurements of Semiconductor Films, and Application to Photoelectrochemical Water-Splitting. *Sol. Energy Mater. Sol. Cells* **2007**, *91*, 1326−1337.

(32) Pulido Melián, E.; González Díaz, O.; Doña Rodríguez, J. M.; Colón, G.; Navío, J.; Macías, M.; Pérez Peña, J. Effect of Deposition of Silver on Structural Characteristics and Photoactivity of TiO_2-Based Photocatalysts. *Appl. Catal., B* **2012**, *127*, 112−120.

(33) Sobana, N.; Muruganadham, M.; Swaminathan, M. Nano-Ag Particles Doped TiO_2 for Efficient Photodegradation of Direct Azo Dyes. *J. Mol. Catal. A: Chem.* **2006**, *258*, 124−132.

DOI: 10.1021/acsami.5b03535
ACS Appl. Mater. Interfaces 2015, 7, 17061−17069

(34) Xiang, Q.; Meng, G. F.; Zhao, H. B.; Zhang, Y.; Li, H.; Ma, W. J.; Xu, J. Q. Au Nanoparticle Modified WO_3 Nanorods with Their Enhanced Properties for Photocatalysis and Gas Sensing. *J. Phys. Chem. C* **2010**, *114*, 2049−2055.
(35) Gyawali, G.; Adhikari, R.; Joshi, B.; Kim, T. H.; Rodríguez-González, V.; Lee, S. W. Sonochemical Synthesis of Solar-Light-Driven Ag-$PbMoO_4$ Photocatalyst. *J. Hazard. Mater.* **2013**, *263*, 45−51.
(36) Niu, J.; Ding, S.; Zhang, L.; Zhao, J.; Feng, C. Visible-Light-Mediated Sr-Bi_2O_3 Photocatalysis of Tetracycline: Kinetics, Mechanisms and Toxicity Assessment. *Chemosphere* **2013**, *93*, 1−8.
(37) Khan, M. M.; Ansari, S. A.; Lee, J.-H.; Ansari, M. O.; Lee, J.; Cho, M. H. Electrochemically Active Biofilm Assisted Synthesis of Ag@CeO_2 Nanocomposites for Antimicrobial Activity, Photocatalysis and Photoelectrodes. *J. Colloid Interface Sci.* **2014**, *431*, 255−263.
(38) Zhang, W.-D.; Jiang, L.-C.; Ye, J.-S. Photoelectrochemical Study on Charge Transfer Properties of ZnO Nanowires Promoted by Carbon Nanotubes. *J. Phys. Chem. C* **2009**, *113*, 16247−16253.
(39) Zhao, W.; Wang, Y.; Yang, Y.; Tang, J.; Yang, Y. Carbon Spheres Supported Visible-Light-Driven CuO-$BiVO_4$ Heterojunction: Preparation, Characterization, and Photocatalytic Properties. *Appl. Catal., B* **2012**, *115−116*, 90−99.
(40) Wang, Z.; Ma, W.; Chen, C.; Ji, H.; Zhao, J. Probing Paramagnetic Species in Titania-Based Heterogeneous Photocatalysis by Electron Spin Resonance (ESR) Spectroscopy-A Mini Review. *Chem. Eng. J.* **2011**, *170*, 353−362.
(41) Sun, L.; Yao, Y.; Wang, L.; Mao, Y.; Huang, Z.; Yao, D.; Lu, W.; Chen, W. Efficient Removal of Dyes Using Activated Carbon Fibers Coupled with 8-hydroxyquinoline Ferric as A Reusable Fenton-Like Catalyst. *Chem. Eng. J.* **2014**, *240*, 413−419.
(42) Zhang, Y.; Yuan, S.; Zhao, Y.; Wang, H.; He, C. Synthesis of Novel Yttrium-doped Graphene Oxide Nanocomposite for Dye Removal. *J. Mater. Chem. A* **2014**, *2*, 7897−7903.
(43) Hou, J.; Wang, Z.; Yang, C.; Zhou, W.; Jiao, S.; Zhu, H. Hierarchically Plasmonic Z-Scheme Photocatalyst of Ag/AgCl Nanocrystals Decorated Mesoporous Single-Crystalline Metastable $Bi_{20}TiO_{32}$ Nanosheets. *J. Phys. Chem. C* **2013**, *117*, 5132−5141.
(44) Ren, J.; Wang, W.; Sun, S.; Zhang, L.; Chang, J. Enhanced Photocatalytic Activity of Bi_2WO_6 Loaded with Ag Nanoparticles under Visible Light Irradiation. *Appl. Catal., B* **2009**, *92*, 50−55.
(45) Guo, Y.; Chen, L.; Ma, F.; Zhang, S.; Yang, Y.; Yuan, X.; Guo, Y. Efficient Degradation of Tetrabromobisphenol A by Heterostructured Ag/$Bi_5Nb_3O_{15}$ Material under the Simulated Sunlight Irradiation. *J. Hazard. Mater.* **2011**, *189*, 614−618.
(46) Wang, X.; Li, S.; Ma, Y.; Yu, H.; Yu, J. $H_2WO_4{\cdot}H_2O$/Ag/AgCl Composite Nanoplates: A Plasmonic Z-Scheme Visible-Light Photocatalyst. *J. Phys. Chem. C* **2011**, *115*, 14648−14655.
(47) Xiao, X.; Ge, L.; Han, C.; Li, Y.; Zhao, Z.; Xin, Y.; Fang, S.; Wu, L.; Qiu, P. A Facile Way to Synthesize Ag@AgBr Cubic Cages with Efficient Visible-Light-Induced Photocatalytic Activity. *Appl. Catal., B* **2015**, *163*, 564−572.
(48) Tada, H.; Kiyonaga, T.; Naya, S. Rational Design and Applications of Highly Efficient Reaction Systems Photocatalyzed by Noble Metal Nanoparticle-Loaded Titanium(IV) Dioxide. *Chem. Soc. Rev.* **2009**, *38*, 1849−1858.
(49) Subramanian, V.; Wolf, E. E.; Kamat, P. V. Catalysis with TiO_2/Gold Nanocomposites. Effect of Metal Particle Size on the Fermi Level Equilibration. *J. Am. Chem. Soc.* **2004**, *126*, 4943−4950.
(50) Wang, D.; Xue, G.; Zhen, Y.; Fu, F.; Li, D. Monodispersed Ag nanoparticles loaded on the Surface of Spherical Bi_2WO_6 Nanoarchitectures with Enhanced Photocatalytic Activities. *J. Mater. Chem.* **2012**, *22*, 4751−4758.
(51) Hirakawa, T.; Kamat, P. V. Charge Separation and Catalytic Activity of Ag@TiO_2 Core-Shell Composite Clusters under UV-Irradiation. *J. Am. Chem. Soc.* **2005**, *127*, 3928−3934.

DOI: 10.1021/acsami.5b03535
ACS Appl. Mater. Interfaces 2015, 7, 17061−17069